Imaging pinning and expulsion of individual superconducting vortices in amorphous MoSi thin films

L. Ceccarelli,[1] D. Vasyukov,[1] M. Wyss,[1,2] G. Romagnoli,[1] N. Rossi,[1,2] L. Moser,[1] and M. Poggio[1,2]
[1]*Department of Physics, University of Basel, 4056 Basel, Switzerland*
[2]*Swiss Nanoscience Institute, University of Basel, 4056 Basel, Switzerland*

(Received 16 July 2019; published 5 September 2019)

We use a scanning nanometer-scale superconducting quantum interference device (SQUID) to image individual vortices in amorphous superconducting MoSi thin films. Spatially resolved measurements of the magnetic field generated by both vortices and Meissner screening satisfy the Pearl model for vortices in thin films and yield values for the Pearl length and bulk penetration depth at 4.2 K. Flux pinning is observed and quantified through measurements of vortex motion driven by both applied currents and thermal activation. The effects of pinning are also observed in metastable vortex configurations, which form as the applied magnetic field is reduced and magnetic flux is expelled from the film. Understanding and controlling vortex dynamics in amorphous thin films is crucial for optimizing devices such as superconducting nanowire single photon detectors (SNSPDs), the most efficient of which are made from MoSi, WSi, and MoGe.

DOI: 10.1103/PhysRevB.100.104504

I. INTRODUCTION

The dynamics of quantized vortices play a crucial role in determining the electronic properties of devices made from type-II superconductors. The dissipative motion of vortices, driven by flowing electrical current, destroys the material's ability to carry current with zero resistance. By controlling the pinning of vortices, they can be immobilized, thereby restoring the superconducting state. Optimized pinning [1–9] and other methods of arresting vortex motion [10] have been used to extend the coherent dissipation-free superconducting state to high critical current densities, fields, and temperatures. The microwave response of superconductors is also affected by the high-frequency dynamics of vortices [11]. Vortex trapping contributes to loss in microwave resonators and conditions the performance of the circuits used as qubits in superconducting quantum computers [12]. Evidence has also emerged that superconducting vortices play a significant role in superconducting nanowire single photon detectors (SNSPDs) [13], whose high speed, detection efficiency, and low dark count rates make them attractive for a wide variety of applications. In particular, vortices are likely involved in both the mechanism used for the detection of photons and in the generation of dark counts.

Here, we image individual superconducting vortices in thin-film MoSi using a scanning nanometer-scale superconducting quantum interference device (SQUID). Spatial maps of the magnetic field above patterned MoSi wires are collected as a function of applied field and reveal the presence of individual vortices and their pinning sites. Measured field profiles fit well to the Pearl model and yield the bulk London penetration depth $\lambda_L = 510 \pm 10$ nm at 4.2 K, which agrees with previous transport measurements of similar films [14]. Pinning sites of various strengths strongly affect the configuration of vortices. In particular, upon the reduction of the applied field, they hinder the expulsion of magnetic field from the film, resulting in long-lasting metastable vortex configurations. The results suggest that improved control of the density and strength of these pinning sites could be important for the optimization of devices based on amorphous MoSi films.

II. EXPERIMENTAL SETUP

We investigate a 65 ± 5-nm-thick film of amorphous $Mo_{0.76}Si_{0.24}$ which is patterned into 9-μm-wide strips with short sections of narrower width, as shown in Fig. 1(b). Similar MoSi nanowires have recently been used as SNSPDs with some of the highest reported detection efficiencies [15]. The composition and thickness are chosen in order to maximize the critical temperature T_c while obtaining an amorphous film with low defect densities and weak pinning effects [14], as desired in most applications.

We use a scanning SQUID-on-tip (SOT) sensor [16,17] to map the component of the magnetic field perpendicular to the MoSi film as a function of position and applied field at 4.2 K. The SOT used here has an effective diameter of 310 nm, as extracted from measurements of the critical current I_{SOT} as a function of a uniform magnetic field applied perpendicular to the SQUID loop $\mathbf{B_a} = B_a\hat{\mathbf{z}}$ [18]. The MoSi sample is mounted below the SOT sensor in a plane parallel to the SQUID loop and perpendicular to $\mathbf{B_a}$. Since the SOT's current response is proportional to the magnetic flux threading through it, it provides a measure of the z-component of the local magnetic field B_z integrated over the loop at its apex. By scanning the sample below the SOT at constant tip-sample spacing z, we map the local magnetic field $B_z(x, y)$. The sub-μm resolution is limited by the spacing and, ultimately, the SOT diameter.

III. VORTEX IMAGING

Before imaging $B_z(x, y)$ generated by the film, we nucleate the vortices by cooling the sample through its measured $T_c = 7.2$ K down to 4.2 K in an externally applied field $\mathbf{B_a}$. This field-cooling process causes flux penetrating the film above T_c to concentrate in the form of quantized vortices which are trapped within the sample as it cools. The trapping potential

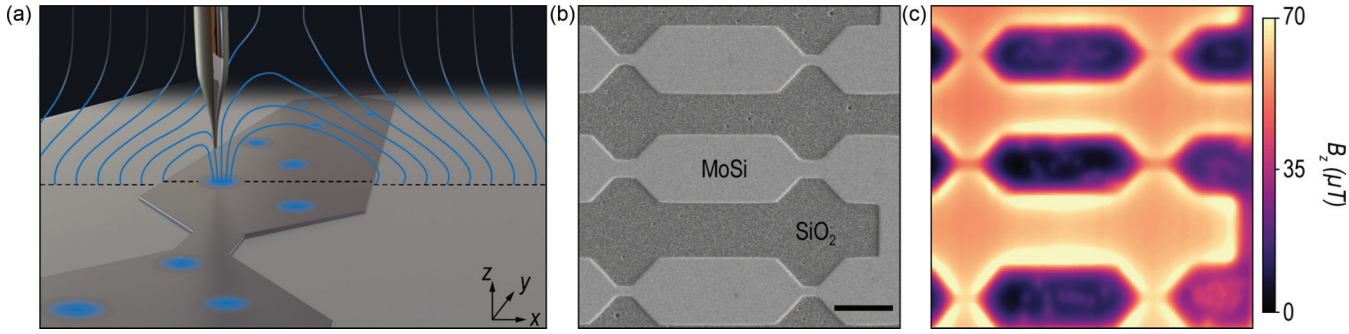

FIG. 1. Setup and MoSi sample. (a) Schematic diagram of scanning SOT tip above superconducting MoSi wire with vortices. (b) Scanning electron micrograph (SEM) and (c) scanning SQUID image of the investigated region. Color-scale contrast in (c) corresponds to the out-of-plane magnetic field $B_z(x, y)$ measured by the SOT in an out-of-plane applied field of $B_a = 1.5\,\mathrm{mT}$. Dark areas of low B_z are due to the Meissner screening of the MoSi film, while bright dots indicate the penetration of flux in the form of superconducting vortices. Scale bar: 10 μm.

is the result of the geometrical barrier produced by extended Meissner screening currents flowing near the sample edges [19]. Figure 1(c) is a typical wide-field image of $B_z(x, y)$ at a fixed tip-sample spacing of $z = 705$ nm, showing the Meissner screening (dark regions) and the presence of a few trapped vortices (bright spots).

In Fig. 2(a), more detailed maps of $B_z(x, y)$ taken after field cooling at $B_a = 0.5$ mT show a few isolated vortices. Line cuts across the MoSi wire through the center of a single vortex are shown for different z in Fig. 2(b), and the dependence of the field as a function of z directly above the vortex is shown in Fig. 2(c). These data are well fit by a model considering both the Meissner screening of the film [20] and the field produced by a perpendicular vortex in a film such that its thickness $t \ll \lambda_L$ (thin-film limit) [21], as first described by Pearl [22] and Carneiro and Brandt [23] (see Appendix D). Fits to these two effects measured at different z allow us to independently determine the Pearl length $\Lambda = 2\lambda_L{}^2/t$, and thus λ_L, as well as the real tip-sample spacing z for each measurement. At 4.2 K, we find $\Lambda = 8.1 \pm 0.9\,\mu$m and a bulk $\lambda_L = 510 \pm 10$ nm, which agrees with measurements by Kubo of films with similar concentration and thickness [14].

IV. VORTEX TRAPPING AND EXPULSION

By field cooling with different values of B_a, we initialize different vortex densities in the MoSi film, as shown in Fig. 3.

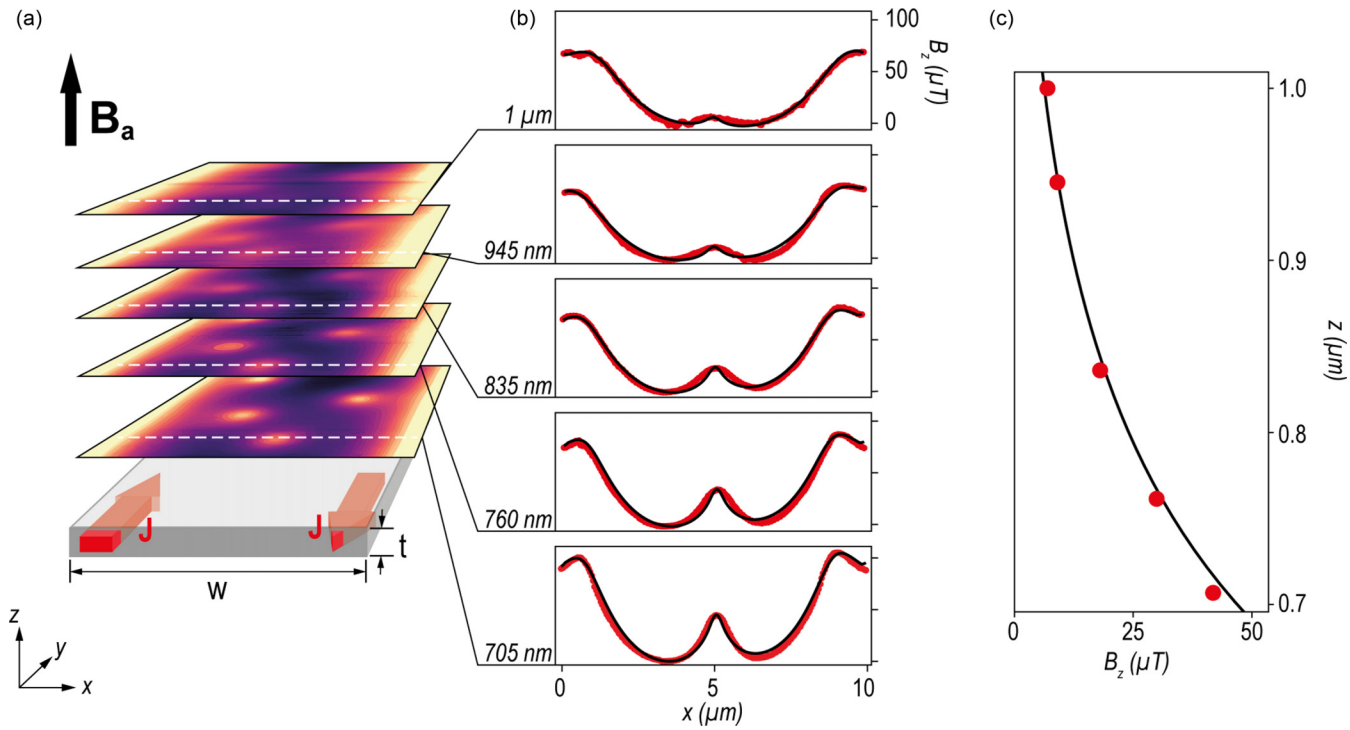

FIG. 2. Fits to Pearl and Meissner models. (a) Schematic drawing of the MoSi wire with 2D measurements of $B_z(x, y)$ and (b) line cuts of $B_z(x)$ through a single vortex at different z (labeled) after field cooling at $B_a = 0.5\,\mathrm{mT}$. (c) Magnetic field directly above the vortex as a function of the tip-sample distance z, $B_z(z)$. Red dots in (b) and (c) represent measurements and black lines fits (see Appendix D).

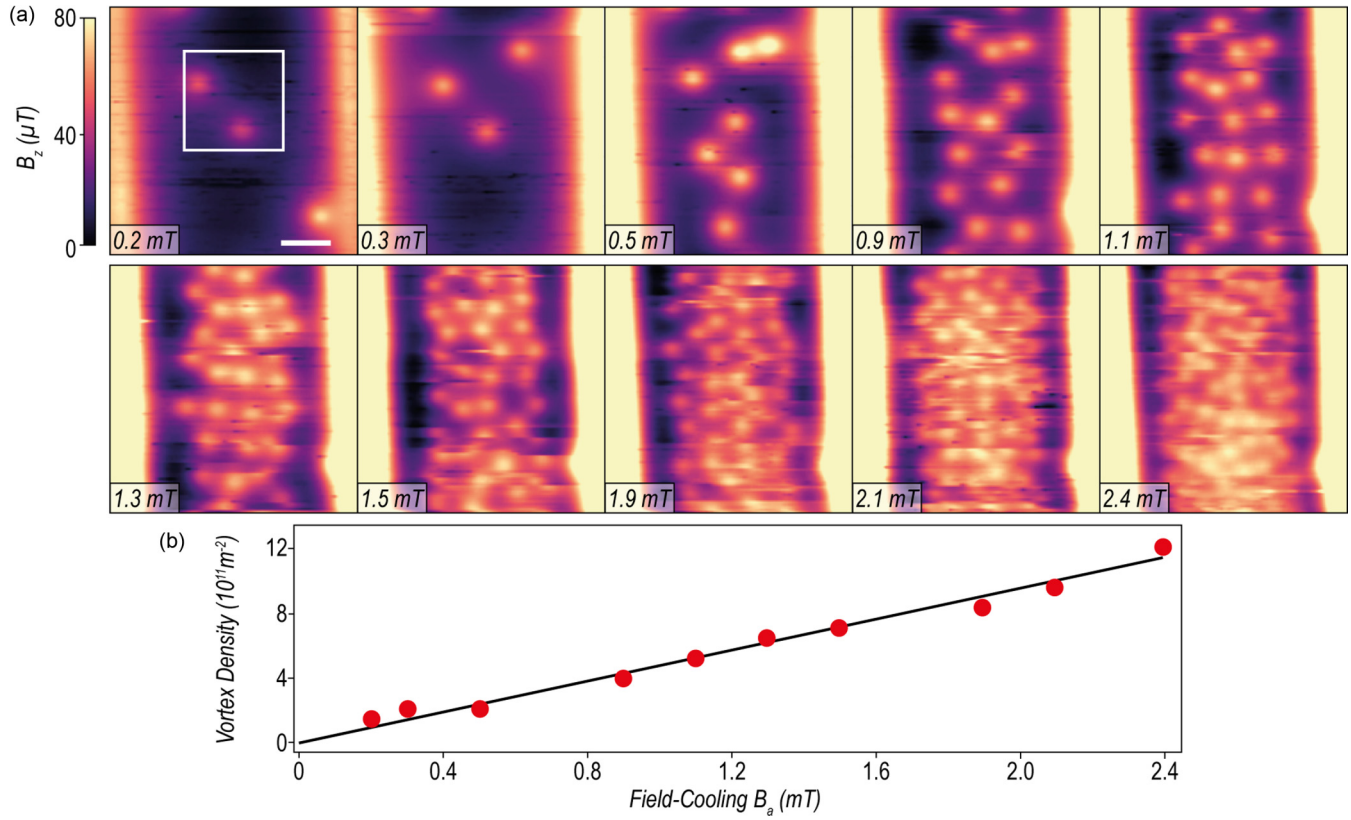

FIG. 3. Vortex density as a function of applied field. (a) Maps of $B_z(x, y)$ taken at $z = 705$ nm over a MoSi wire segment after field cooling with increasing B_a, shown in the bottom-left corner of each image. Scale bar: 2 μm. (b) Vortex density in a 4×4 μm area at the center of the MoSi wire, delineated by the white box in (a), plotted as a function of the field-cooling field B_a. Data are shown as red dots, while the expected B_a/Φ_0 dependence is shown as a black line.

In the central region of the widest part of the wire, the measured vortex density depends linearly on B_a with slope given by ${\Phi_0}^{-1}$, where $\Phi_0 = h/(2e)$ is the magnetic flux quantum, h is Planck's constant, and e is the elementary charge. In fact, the density should go as $(B_a - B_K)/\Phi_0$, where B_K is a critical induction below which no vortex trapping occurs, but because $B_K \ll B_a$ in our experiments, the measured results match theoretical predictions [24] as well as previous measurements in similar Nb [25], yttrium barium copper oxide (YBCO) [24], and Pb [26] wires. This behavior corresponds to the vortex density expected when the total flux through the film above T_c nucleates into vortices and is trapped within the film. However, when the entire area of the MoSi wire is considered, including the edges, the measured vortex density is significantly less than the full above-T_c flux density. The images of $B_z(x, y)$ in Fig. 3(a) show vortex-free regions near the sample edges, which shrink with increasing B_a, as also observed in Pb films by Embon *et al.* [27]. This nonuniform vortex density, which is concentrated in the center of the wire, reflects the reduced effective width compared to the wire width, in which vortices can be trapped by the Meissner screening currents. In thin-film wires whose width $w \gg t$, the screening current density decreases slowly from the edges, pushing vortices into the central part of the wire [19,27–29]. As a result, flux threading the sample near its edges above T_c is subsequently expelled upon cooldown.

In order to investigate the potential trapping the vortices, after field cooling we image the vortex configuration upon the reduction of B_a. The left panel of Fig. 4(a) shows an image of $B_z(x, y)$ after field cooling at $B_a = 2.8$ mT to 4.2 K. The panels on the right show the same region immediately after ramping the applied field down to lower B_a at constant temperature. In the case shown in the top half of Fig. 4(a), the field is ramped down $B_a = 0.5$ mT in 30 s and the 10×10-μm^2 image is taken line-by-line in a total time of 260 s with x as the fast axis. Towards the end of the image, after 200 s, we observe a sudden change of the vortex configuration. The system goes from an "inflated" state, in which vortices appear in the previously unoccupied edge region, to a state similar to that observed after field cooling, containing fewer trapped vortices and vortex-free edges. Upon further repeated imaging, the second configuration is always observed, except for small changes due to thermally activated vortex hopping, which will be discussed in the next section. In the bottom half of Fig. 4(a), the field is reduced in three steps to $B_a = 0.2$ mT, with similar discontinuities marking a transition between "inflated" and equilibrium states showing up in the images taken at $B_a = 1.9$ and 0.8 mT. The panels of Fig. 4(b), showing a 8.25×8.25-μm^2 view of $B_z(x, y)$ near the wire edge, display similar behavior 190 s after B_a is reduced from 1.5 to 1.0 mT and 320 s after it is subsequently reduced to 0.5 mT. In particular, we note that in the inflated states observed at 1.0

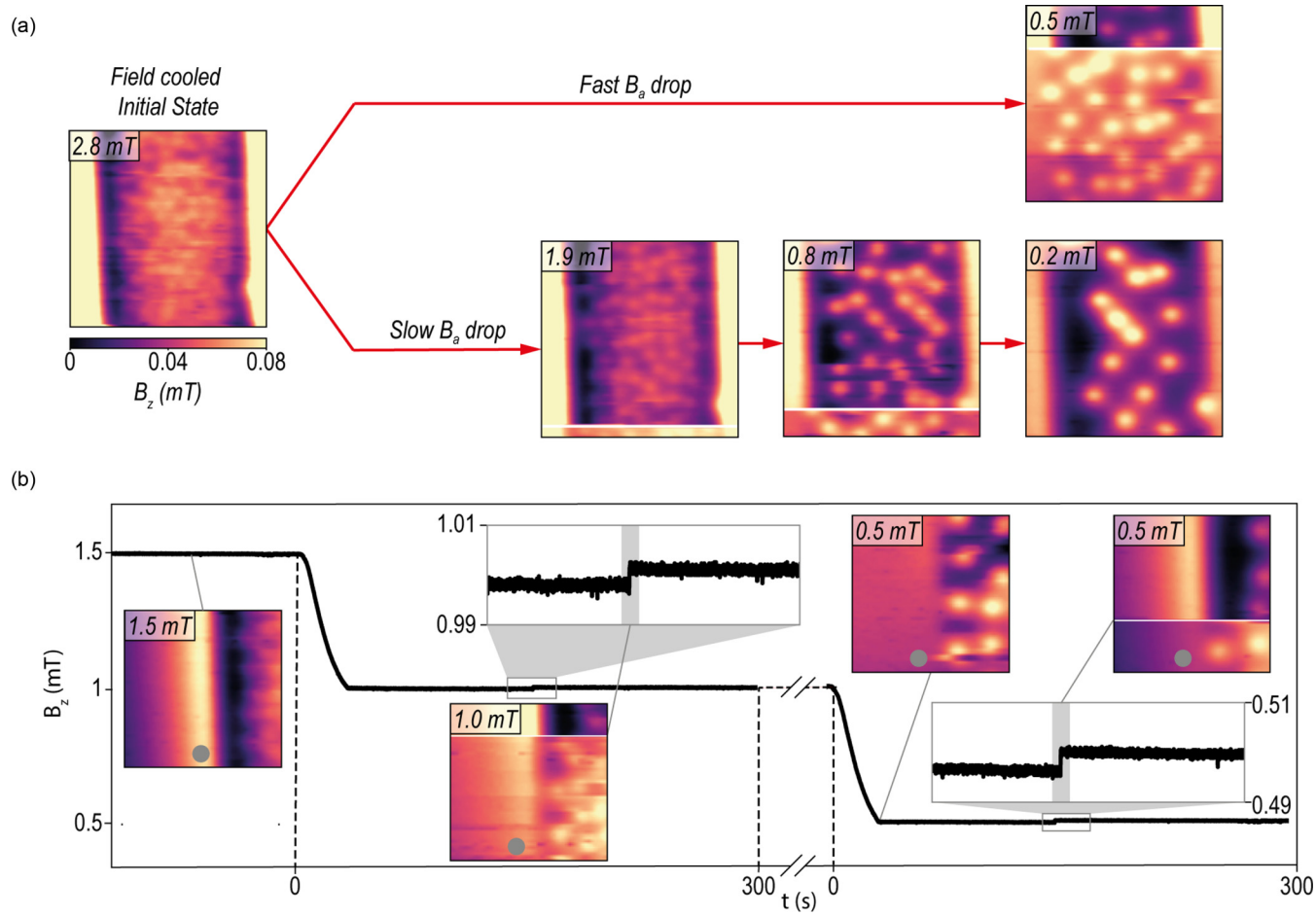

FIG. 4. "Inflated" metastable vortex configurations. (a) Left image shows a map of $B_z(x, y)$ 705 nm over a MoSi wire segment after field cooling at $B_a = 2.8$ mT. The image on the top right shows a measurement of the same area immediately after a decrease of B_a to 0.5 mT in 30 s. The 10×10-μm^2 images are taken line-by-line in a total time of 260 s, with x as the fast axis (71 lines at 3.7 s/line). The white line represents the moment at which we observe a discontinuous change in the vortex configuration. The bottom-right images are taken at three fields as B_a is reduced from 2.8 to 0.2 mT. (b) 8.25×8.25-μm^2 images of $B_z(x, y)$ near the wire edge, each taken in a total time of 245 s (51 lines at 4.8 s/line). (b) The leftmost image shows the configuration after field cooling at $B_a = 1.5$ mT. Other images show subsequent configurations after decreasing B_a to 1 mT and then to 0.5 mT. The plot displays B_z as a function of time at the position indicated by the gray circle, showing both the reduction in B_a and the signatures of vortex expulsion, which are highlighted in the zoomed-in sections. Note that the flux measured at this position (gray circle) and the spatial maps do not correspond to simultaneous measurements; they correspond to measurements carried out under the same initialization conditions. Therefore, the gray lines connecting the 2D maps to various points along the plot are meant to indicate similar events in different experimental runs, not two measurements of the same event.

and 0.5 mT, the vortices in the edge region appear pinned to the same set of pinning sites. Such vortex expulsion behavior is observed repeatedly for similar intervals of B_a and over similar time scales at constant temperature.

To confirm that transitions from the inflated state to the final state are not induced by interactions with our scanning tip [30], we carry out the same measurements with the SOT at a fixed position, just outside the edge of the sample, as marked by the gray circles in Fig. 4(b). Once again, B_a is reduced at a constant temperature and the resulting field B_z next to the wire is plotted as a function of time in the main part of Fig. 4(b). After the initial reduction due to the ramping down of B_a, B_z is constant until around 150 s, when it increases in a sudden step. This increase corresponds to the expulsion of the extra vortices present in the inflated state. Vortex expulsion with similar time scales is observed upon repeated experiments and for different fields. Since this behavior corresponds to what was observed in the scanning experiments, we rule out interactions with the tip as the trigger for the observed flux expulsion. Although strong interactions were previously observed between vortices in YBCO and a magnetic force microscopy tip [30], the much weaker stray fields produced by our SOT tip produce a negligible perturbation to each vortex, calculated to be less than 10 fN following the procedure described by Embon *et al.* [26].

The observation of a metastable inflated state, which lasts on the order of a hundred of seconds before flux expulsion and relaxation to the equilibrium configuration, points to the presence of pinning sites and thermally activated vortex hopping. The presence of vortices near the edges in the metastable state cannot be accounted for by the trapping potential provided by Meissner currents: this potential only traps vortices in the middle of the wire, with its barrier occupying the region near the edges. The vortices near the edges can be immobilized

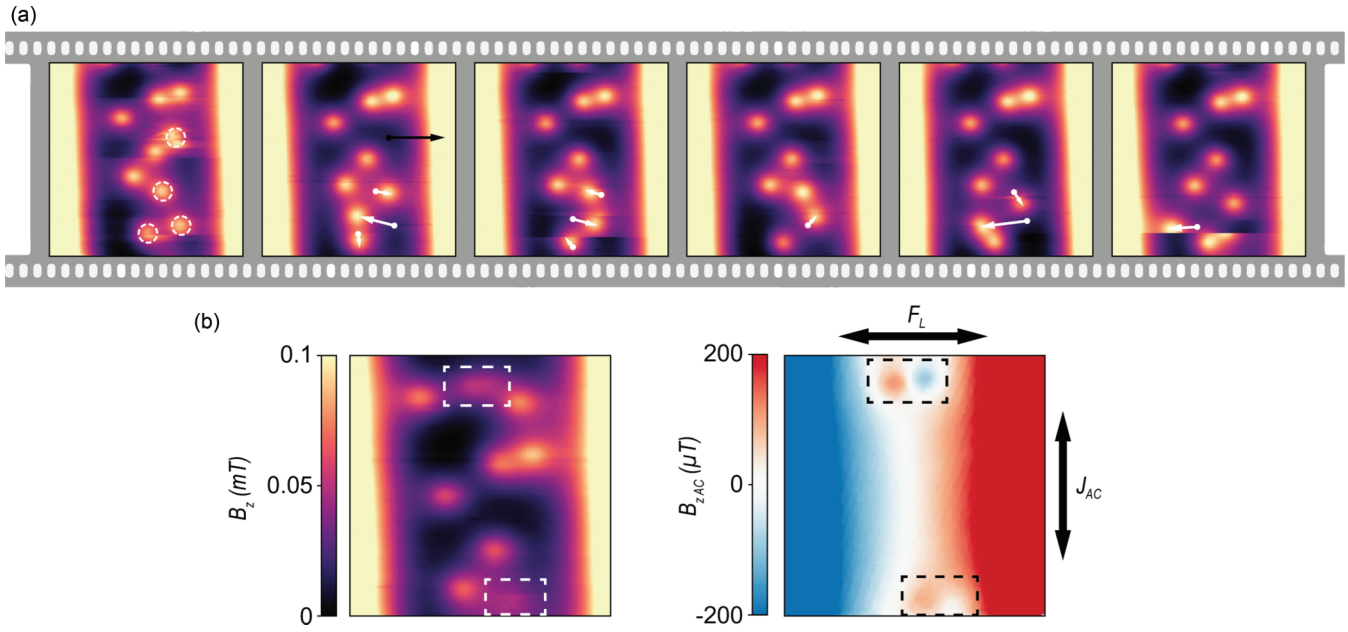

FIG. 5. Thermally activated vortex hopping and pinning strength. (a) Maps of $B_z(x, y)$ at $z = 705$ nm over a MoSi wire segment after field cooling with $B_a = 0.8$ mT. Each 10×10-μm^2 image is of the same region and is taken one after the other line-by-line in 260 s with x as the fast axis (71 lines at 3.7 s/line). Circles and arrows highlight vortices hopping between neighboring pinning sites. (b) Left image is a map of $B_z(x, y)$ under the same conditions but in the additional presence of an ac applied current along $\hat{y}$, producing a F_{ac} along $\hat{x}$. The right image shows $B_{z,ac}(x, y)$, which is measured simultaneously. The highlighted areas show vortices which oscillate as a result of F_{ac}. Scan area $10 \times 10\,\mu$m^2.

only by pinning sites. These potential wells, however, are not deep enough to completely freeze the vortex motion at 4.2 K and, due to thermally activated vortex hopping, the edge vortices are eventually expelled as the sample relaxes to its equilibrium configuration.

V. PINNING SITES

The presence of thermally activated vortex hopping at 4.2 K is evident from repeated imaging of $B_z(x, y)$ at equilibrium. As shown in Fig. 5(a), certain vortices are seen to jump between neighboring pinning sites within a single image or between successive images. The former effect is evident in the discontinuities between one x line and the next, while the latter can be seen when a vortex changes position between images. These jumps occur on a time scale ranging from a few to a few hundred seconds. Given this time scale and the similar time scale of the metastable configuration held together by pinning sites at the sample edges, we estimate the depth of these pinning potentials E_{pin} using the Boltzmann formula for a thermally activated hopping rate: $\nu_{hop} = \nu_0 e^{-(\frac{E_{pin}}{k_B T})}$, where k_B is the Boltzmann constant, T is the temperature, and ν_0 is the attempt frequency. Solving for E_{pin}, we find an energy between 4 and 12 meV, whose uncertainty results from the imprecisely known ratio of $\frac{\nu_0}{\nu_{hop}}$ (ν_{hop} ranges from a few mHz to 1 Hz, while ν_0 is assumed to lie between 10^5 and 10^{12} Hz [31,32]). These weak pinning sites are therefore not strong enough to freeze vortex motion at 4.2 K and thus provide a path through which the system can eventually find its equilibrium configuration. As B_a is increased, we note that pinning sites displaying thermally activated hopping occur more frequently from 25% of pinning sites at $B_a = 0.6$ mT to up to 85% at $B_a = 1.5$ mT (see Appendix E). As the vortex density increases, stronger vortex-vortex interactions, which have a long-range $1/r$ force in thin films, destabilize an increasing number of vortex pinning sites.

Although many pinning sites exhibit thermally activated vortex hopping, some sites do not, pointing to deeper trapping potentials. We further investigate these sites by driving vortex motion using an ac current I_{ac} applied along the y direction (long direction of the wire). This current results in an ac Lorentz force $F_{ac} = \frac{I_{ac}}{w}\Phi_0$ on each vortex along the x direction. F_{ac} drives oscillations of the vortices around their equilibrium positions. The resulting motion can be measured using the scanning SOT as either a blurred vortex image in $B_z(x, y)$, as shown in the left panel of Fig. 5(b), or, more clearly, as a dipolar signal in the magnetic field produced by the sample at the frequency of the ac current drive $B_{z,ac}(x, y)$, as shown in the right panel [26]. The amplitude of this signal reflects the size of the oscillation and the gradient of the static field $B_z(x, y)$ produced by the vortex.

Vortices at different pinning sites respond differently to F_{ac}, indicating the varying strength of the pinning potentials throughout the sample. At $B_a = 0.9$ mT, weak pinning sites (30%), showing thermally activated hopping, are induced to jump from site to site by F_{ac} with amplitudes in the 100-fN range. Strong pinning sites (50%) show no measurable response to this F_{ac}. Intermediate pinning potentials (20%) show oscillatory responses to the F_{ac}. From the strength of F_{ac}, we extract effective pinning spring constants of around 0.6 μN/m. Compared to similar measurements in Pb films, these potentials are 100 times shallower (less curvature),

indicating their larger spatial extent and weaker strength. By increasing Lorentz force up to a maximum value $F_{ac,max}$ at which these vortices escape from their pinning sites, we can integrate and estimate the depth of the potential well, typically obtaining $E_{pin} \sim 60$ meV.

Together, our results point to a range of E_{pin} from a few meV up to at least tens of meV, excluding the pinning sites that do not respond to thermal or Lorentz perturbations. As expected, these values are a fraction of the estimated condensation energy of the vortex core in this sample of $\frac{H_c^2}{2\,\mu_0}\pi\xi^2 t = 110$ meV, where $\xi = 7$ nm is the coherence length derived from a measurement of the upper critical field $H_{c2} = \frac{\Phi_0}{2\,\pi\xi^2} = 6.8$ T [14], $H_c = \frac{\Phi_0}{\sqrt{8}\,\pi\lambda_L\xi} = 66$ mT is the thermodynamic critical field, and μ_0 is the permeability of free space.

If we exclude the weak thermally activated pinning sites, we also find that the vortices are always driven in phase with F_{ac} and along the direction of the drive (x direction). This behavior points to isotropic conservative trapping potentials, which are sparsely distributed, i.e., large pinning centers that do not overlap. These large and well-separated pinning centers contrast the observations made by Embon *et al.* in similar experiments on Pb thin films [26]. There, vortices displayed anisotropic responses and spring softening upon driving with Lorentz forces, because pinning centers were close enough to form complex, anisotropic potentials for vortices. Those data were well-described by a computational model that included small clusters of pinning defects separated on the order of a superconducting coherence length. Our results also differ from recent scanning SQUID susceptibility measurements in the layered superconductor FeSe, which revealed weak and highly anisotropic pinning potentials, constraining vortex motion predominantly along twin boundaries [33].

The vortex pinning potentials observed in our MoSi films are likely the result of either crystalline precipitates within the amorphous alloy, structural defects, or local variations in the thickness and elemental composition. Given the presence of visible inclusions and roughness of varying sizes observed by scanning electron microscopy (SEM) of our sample [18], structural defects and thickness variations are the most probable causes. In fact, by comparing $B_z(x, y)$ images of vortices with SEM of the same part of the sample, we correlate some of the strongest pinning centers, which do not respond to either thermal or Lorentz perturbations, with pockmarks, perhaps representing perforations, on the surface of the film. The films may also have small inhomogeneities in Si concentration, which would result in local changes of λ_L [14] and thus potential pinning sites. The presence of such inhomogeneities in thickness or composition could explain some slight differences in the maximum observed fields produced by different vortices. Precipitates are typically a limiting factor in much thicker films, which require long sputtering times for deposition [14].

VI. CONCLUSIONS

Our scanning SOT experiments, because of the sensor's combination of high spatial resolution and high magnetic field sensitivity, reveal images of individual superconducting Pearl vortices in amorphous MoSi thin films. In addition to providing a measure of the penetration depth of the film, we directly observe their thermally activated hopping at 4.2 K. Since the vortices are not completely frozen onto their pinning sites, we are able to estimate the depth of the weakest pinning potentials and observe metastable vortex configurations present for tens of seconds before the system reaches equilibrium.

The dynamic nature of the vortex configurations in MoSi at 4.2 K may have implications for SNSPDs and other devices fabricated from such films. The thermally activated vortex hopping observed here may be a source of residual dark counts in SNSPDs. Our experiments also make plain the necessity of further reducing the density of unintentional pinning sites by improving sample quality. In order to aid in the optimization of MoSi-based superconducting devices, future scanning SQUID studies should aim to study different MoSi films grown under different conditions.

ACKNOWLEDGMENTS

We thank Prof. Christian Schönenberger, Prof. Richard Warburton, and Daniel Sacker for guidance in the fabrication of the MoSi samples. We also thank the machine shop of the Department of Physics and Dr. Monica Schönenberger and the Nano Imaging Lab for support with part design and AFM, respectively. We acknowledge the support of the Canton Aargau; the ERC Starting Grant NWScan (Grant No. 334767); and the Swiss National Science Foundation via Grants No. 200020-159893 and No. 200020-178863, the Sinergia network Nanoskyrmionics (Grant No. CRSII5-171003), and the NCCR Quantum Science and Technology (QSIT).

APPENDIX A: MOSI SAMPLE FABRICATION

The 65 ± 5-nm-thick $Mo_{0.76}Si_{0.24}$ film is deposited onto an SiO_2 substrate by cosputtering with a DC and rf bias on Mo and Si targets, respectively. The thickness is determined using atomic force microscopy (AFM) and SEM, while the concentrations of Mo and Si are measured by x-ray photoelectron spectroscopy (XPS) [18]. The film is patterned into a series of meandering wires over a 500×500-μm^2 area [18] by a combination of electron-beam lithography and reactive ion etching.

APPENDIX B: SOT SENSOR FABRICATION

The SOT is fabricated by evaporating Pb on the apex of a pulled quartz capillary according to a self-aligned method pioneered by Finkler *et al.* [16] and perfected by Vasyukov *et al.* [17]. The evaporation is carried out in a custom-made evaporator with a base pressure of 2×10^{-8} mbar and a rotatable sample holder cooled by liquid He. In accordance with Halbertal *et al.* [34], an additional Au shunt was deposited close to the tip apex prior to the Pb evaporation for protection of the SOTs against electrostatic discharge. SOTs were characterized in a test setup prior to their use in the scanning probe microscope [18].

APPENDIX C: SCANNING SOT EXPERIMENTS

The SOT and the MoSi sample are mounted in a custom-built scanning probe microscope operating under vacuum

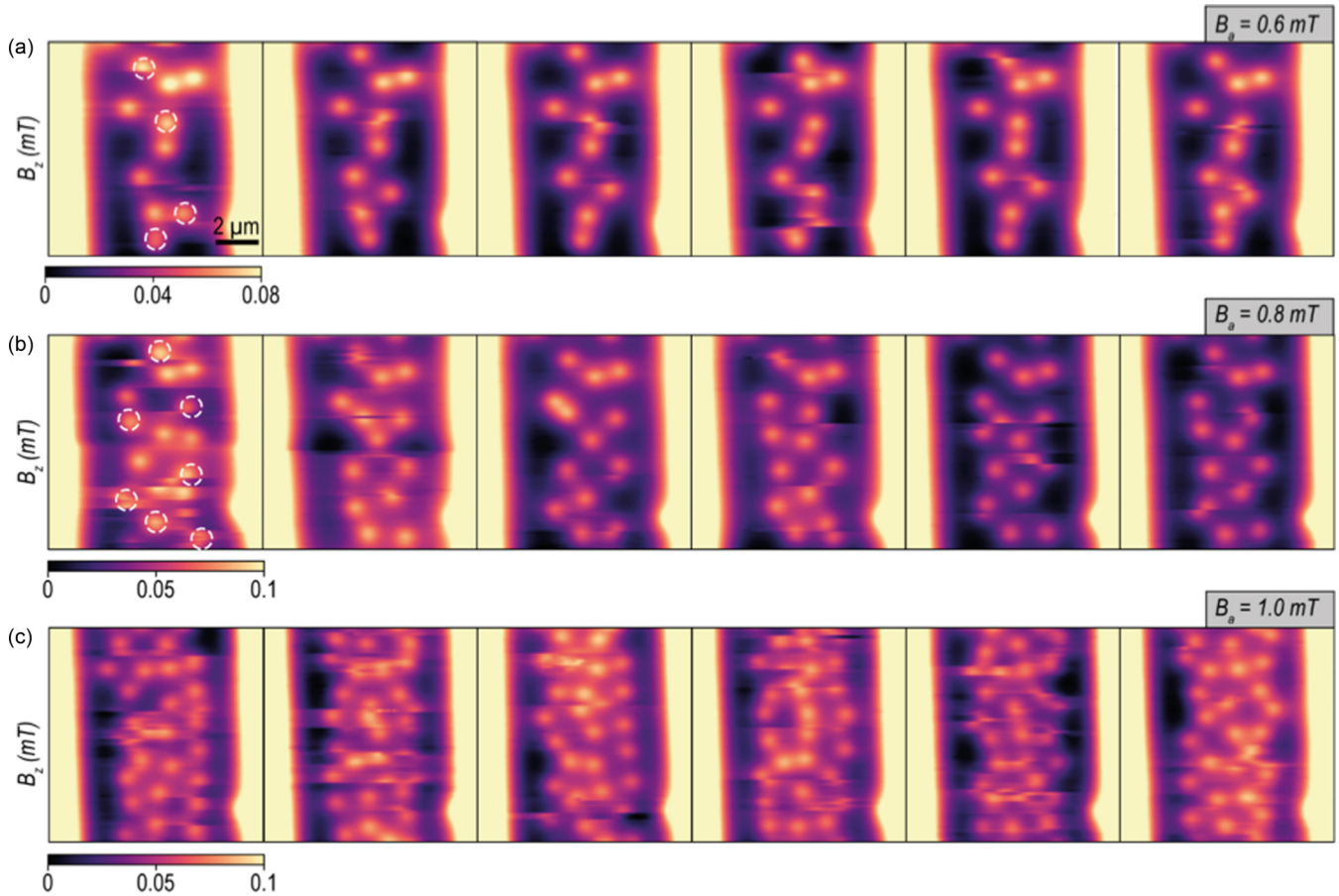

FIG. 6. Dependence of thermally activated vortex hopping on applied field. (a–c) Time series of images of $B_z(x, y)$ taken at three different field-cooling fields B_a. Dashed circles in (a) and (b) highlight vortices which hop in subsequent frames. Given the large proportion of vortices hopping in (c), we do not highlight them there.

in a ^{4}He cryostat [35]. A serial SQUID array amplifier is used to measure the current flowing through the SOT [18]. Positioning and scanning of the sample below the SOT is carried out using piezoelectric positioners and scanners (Attocube AG). In order to aid in positioning the sensor over the area of interest at low temperature, we pass ac electric currents through the meandering wires patterned in the MoSi [18]. The SOT's sensitivity to the resulting Biot-Savart fields allows us to navigate across the sample. In addition, close to the surface, the distortion of the local DC magnetic field by the Meissner effect helps to determine the sensor's position, e.g., as shown in Fig. 1(c). All measurements were performed in open-loop mode at constant spacing above the sample.

APPENDIX D: MODEL FOR MAGNETIC FIELD ABOVE THIN-FILM WIRE

The model used to fit the spatial dependence of B_z above the superconducting MoSi wire considers the wire's expulsion of flux due to the Meissner effect and the field produced by a superconducting vortex in the Pearl limit. By summing the resulting field profiles, we model the 1D profile shown in Figs. 2(b) and 2(c), which cut through the center of the field produced by a single vortex in the wire.

The model for the field produced by Meissner screening follows Brisbois *et al.* [20]:

$$B_{z,\mathrm{Meissner}}(x,z) = 1 + \frac{1}{\pi}\int_{-\frac{w}{2}}^{\frac{w}{2}} \frac{(x-x')x'dx'}{[(x-x')^2+z^2]\sqrt{\left(\left(\frac{w}{2}\right)^2 - x'^2\right) + \frac{8a\lambda_L^2}{\pi t}}}.$$

The model for the field produced by the superconducting vortex is based on Pearl's model, because the wire thickness is much less than the penetration depth ($t \ll \lambda_\mathrm{L}$) [22,23]:

$$B_{z,\mathrm{vortex}}(x,z) = \Phi_0 \int_{-\frac{1}{L}}^{\frac{1}{L}} \frac{d^2k}{4\pi^2} \frac{e^{i\boldsymbol{k}\cdot\boldsymbol{x}}}{1+\frac{4k^2\lambda_L^4}{t^2}} f(k,z),$$

where $f(k,z) = c_1 e^{-kz}$ above the film, i.e., for $z > 0$, where 0 is the surface of the film. c_1 depends on the film thickness t:

$$c_1(k) = [(k+\rho)e^{\rho t} + (k-\rho)e^{-\rho t} - 2k]\frac{\rho}{c_2}$$

$$c_2(k) = (k+\rho)^2 e^{\rho t} - (k-\rho)^2 e^{-\rho t}$$

$$\rho = \sqrt{k^2 + \left(\frac{2\lambda_L{}^2}{t}\right)^{-2}}.$$

The measured field is then fit with the function $B_{z,\mathrm{fit}}(x,z) = B_{z,\mathrm{Meissner}}(x,z) + B_{z,\mathrm{vortex}}(x,z)$, where the London penetration depth λ_L and probe-sample distance z are used as fit parameters. The value of λ_L is found to be 510 ± 10 nm (making the Pearl penetration depth $\Lambda \cong 8$ μm), and the z values are shown in Fig. 2(b) for five different probe-sample distances.

APPENDIX E: EFFECT OF VORTEX DENSITY ON THERMALLY ACTIVATED HOPPING

As the field-cooling field B_a is increased, the proportion of pinning sites showing thermally activated vortex hopping increases. The increasing vortex density results in stronger vortex-vortex interactions, which destabilize more and more vortex pinning sites. This effect can be observed in Fig. 6, which shows three sequences of images taken one after the other for three different field-cooling fields $B_a = 0.6$, 0.8, and 1.0 mT. Each frame requires 153 s to measure, and successive images are taken immediately after the previous image finishes [18]. As shown in Fig. 7, the proportion of pinning sites showing thermally activated vortex hopping, $R = \frac{n_m}{n_t}$, where n_m is the density of vortices showing thermally activated hopping and n_t is the total vortex density, increases with B_a until nearly all vortices show thermally activated behavior.

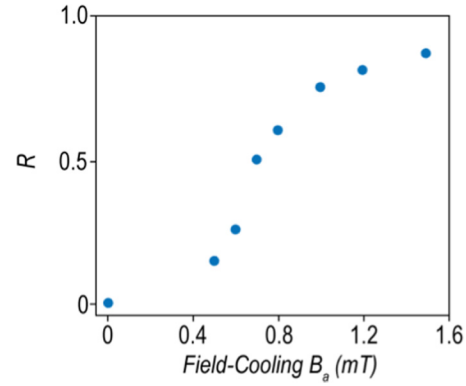

FIG. 7. Proportion vortices showing thermally activated hopping as a function of B_a in measurements like those shown in Fig. 6.

[1] J. L. MacManus-Driscoll, S. R. Foltyn, Q. X. Jia, H. Wang, A. Serquis, L. Civale, B. Maiorov, M. E. Hawley, M. P. Maley, and D. E. Peterson, Nat. Mater. **3**, 439 (2004).

[2] L. Fang, Y. Jia, V. Mishra, C. Chaparro, V. K. Vlasko-Vlasov, A. E. Koshelev, U. Welp, G. W. Crabtree, S. Zhu, N. D. Zhigadlo, S. Katrych, J. Karpinski, and W. K. Kwok, Nat. Commun. **4**, 2655 (2013).

[3] T. Haugan, P. N. Barnes, R. Wheeler, F. Meisenkothen, and M. Sumption, Nature (London) **430**, 867 (2004).

[4] P. Mele, K. Matsumoto, T. Horide, O. Miura, A. Ichinose, M. Mukaida, Y. Yoshida, and S. Horii, Supercond. Sci. Technol. **19**, 44 (2005).

[5] S. Kang, A. Goyal, J. Li, A. A. Gapud, P. M. Martin, L. Heatherly, J. R. Thompson, D. K. Christen, F. A. List, M. Paranthaman, and D. F. Lee, Science **311**, 1911 (2006).

[6] J. Gutiérrez, A. Llordés, J. Gázquez, M. Gibert, N. Romà, S. Ricart, A. Pomar, F. Sandiumenge, N. Mestres, T. Puig, and X. Obradors, Nat. Mater. **6**, 367 (2007).

[7] B. Maiorov, S. A. Baily, H. Zhou, O. Ugurlu, J. A. Kennison, P. C. Dowden, T. G. Holesinger, S. R. Foltyn, and L. Civale, Nat. Mater. **8**, 398 (2009).

[8] A. Llordés, A. Palau, J. Gázquez, M. Coll, R. Vlad, A. Pomar, J. Arbiol, R. Guzmán, S. Ye, V. Rouco, F. Sandiumenge, S. Ricart, T. Puig, M. Varela, D. Chateigner, J. Vanacken, J. Gutiérrez, V. Moshchalkov, G. Deutscher, C. Magen, and X. Obradors, Nat. Mater. **11**, 329 (2012).

[9] S. Lee, C. Tarantini, P. Gao, J. Jiang, J. D. Weiss, F. Kametani, C. M. Folkman, Y. Zhang, X. Q. Pan, E. E. Hellstrom, D. C. Larbalestier, and C. B. Eom, Nat. Mater. **12**, 392 (2013).

[10] R. Córdoba, T. I. Baturina, J. Sesé, A. Y. Mironov, J. M. D. Teresa, M. R. Ibarra, D. A. Nasimov, A. K. Gutakovskii, A. V. Latyshev, I. Guillamón, H. Suderow, S. Vieira, M. R. Baklanov, J. J. Palacios, and V. M. Vinokur, Nat. Commun. **4**, ncomms2437 (2013).

[11] C. Song, T. W. Heitmann, M. P. DeFeo, K. Yu, R. McDermott, M. Neeley, J. M. Martinis, and B. L. T. Plourde, Phys. Rev. B **79**, 174512 (2009).

[12] G. Wendin, Rep. Prog. Phys. **80**, 106001 (2017).

[13] A. Engel, J. Lonsky, X. Zhang, and A. Schilling, IEEE Trans. Appl. Supercond. **25**, 1 (2015).

[14] S. Kubo, J. Appl. Phys. **63**, 2033 (1988).

[15] M. Caloz, M. Perrenoud, C. Autebert, B. Korzh, M. Weiss, C. Schönenberger, R. J. Warburton, H. Zbinden, and F. Bussières, Appl. Phys. Lett. **112**, 061103 (2018).

[16] A. Finkler, Y. Segev, Y. Myasoedov, M. L. Rappaport, L. Ne'eman, D. Vasyukov, E. Zeldov, M. E. Huber, J. Martin, and A. Yacoby, Nano Lett. **10**, 1046 (2010).

[17] D. Vasyukov, Y. Anahory, L. Embon, D. Halbertal, J. Cuppens, L. Neeman, A. Finkler, Y. Segev, Y. Myasoedov, M. L. Rappaport, M. E. Huber, and E. Zeldov, Nat. Nanotechnol. **8**, 639 (2013).

[18] See Supplemental Material at http://link.aps.org/supplemental/10.1103/PhysRevB.100.104504 for a description of SQUID-on-tip characteristics and for measurements of the MoSi sample thickness, surface, and composition.

[19] E. Zeldov, A. I. Larkin, V. B. Geshkenbein, M. Konczykowski, D. Majer, B. Khaykovich, V. M. Vinokur, and H. Shtrikman, Phys. Rev. Lett. **73**, 1428 (1994).

[20] J. Brisbois, B. Raes, J. Van de Vondel, V. V. Moshchalkov, and A. V. Silhanek, J. Appl. Phys. **115**, 103906 (2014).

[21] F. Tafuri, J. R. Kirtley, P. G. Medaglia, P. Orgiani, and G. Balestrino, Phys. Rev. Lett. **92**, 157006 (2004).

[22] J. Pearl, Appl. Phys. Lett. **5**, 65 (1964).

[23] G. Carneiro and E. H. Brandt, Phys. Rev. B **61**, 6370 (2000).

[24] K. H. Kuit, J. R. Kirtley, W. van der Veur, C. G. Molenaar, F. J. G. Roesthuis, A. G. P. Troeman, J. R. Clem, H. Hilgenkamp, H. Rogalla, and J. Flokstra, Phys. Rev. B **77**, 134504 (2008).

[25] G. Stan, S. B. Field, and J. M. Martinis, Phys. Rev. Lett. **92**, 097003 (2004).

[26] L. Embon, Y. Anahory, A. Suhov, D. Halbertal, J. Cuppens, A. Yakovenko, A. Uri, Y. Myasoedov, M. L. Rappaport, M. E. Huber, A. Gurevich, and E. Zeldov, Sci. Rep. **5**, 7598 (2015).

[27] L. Embon, Y. Anahory, Ž. L. Jelić, E. O. Lachman, Y. Myasoedov, M. E. Huber, G. P. Mikitik, A. V. Silhanek, M. V. Milošević, A. Gurevich, and E. Zeldov, Nat. Commun. **8**, 85 (2017).

[28] E. H. Brandt, Phys. Rev. B **59**, 3369 (1999).

[29] E. H. Brandt, G. P. Mikitik, and E. Zeldov, J. Exp. Theor. Phys. **117**, 439 (2013).

[30] O. M. Auslaender, L. Luan, E. W. J. Straver, J. E. Hoffman, N. C. Koshnick, E. Zeldov, D. A. Bonn, R. Liang, W. N. Hardy, and K. A. Moler, Nat. Phys. **5**, 35 (2009).

[31] M. Tinkham, *Introduction to Superconductivity*, 2nd ed. (Dover Publications, Mineola, NY, 2004).

[32] M. Pannetier, Ph. Lecoeur, P. Bernstein, T. D. Doan, and J. F. Hamet, Phys. Rev. B **62**, 15162 (2000).

[33] I. P. Zhang, J. C. Palmstrom, H. Noad, L. Bishop-Van Horn, Y. Iguchi, Z. Cui, E. Mueller, J. R. Kirtley, I. R. Fisher, and K. A. Moler, Phys. Rev. B **100**, 024514 (2019).

[34] D. Halbertal, J. Cuppens, M. B. Shalom, L. Embon, N. Shadmi, Y. Anahory, H. R. Naren, J. Sarkar, A. Uri, Y. Ronen, Y. Myasoedov, L. S. Levitov, E. Joselevich, A. K. Geim, and E. Zeldov, Nature (London) **539**, 407 (2016).

[35] D. Vasyukov, L. Ceccarelli, M. Wyss, B. Gross, A. Schwarb, A. Mehlin, N. Rossi, G. Tütüncüoglu, F. Heimbach, R. R. Zamani, A. Kovács, A. Fontcuberta i Morral, D. Grundler, and M. Poggio, Nano Lett. **18**, 964 (2018).